Design and evaluation of a novel SOFC-driven multi-generation system

SEYED MOHAMMAD SATTARI SADAT[1], **ARASH MIRABDOLAH LAVASANI**[2], **AND HADI GHAEBI**[3]

[1, 2] *Department of Mechanical Engineering, Central Tehran Branch, Islamic Azad University, Tehran, Iran*
[3] *Department of Mechanical Engineering, Faculty of Engineering, University of Mohaghegh Ardabili, Ardabil, Iran*
[*] *Corresponding author: arashlavasani@iauctb.ac.ir*

Manuscript received 1 Janury, 2019;Revised 10 May, 2019, accepted 10 May, 2019. Paper no. JEMT-1811-1137.

Parametric evaluation and thermodynamics first-law examination of a novel multigeneration system, which is comprised of a hybrid solid oxide fuel cell/gas turbine (SOFC/GT) system, a heat recovery heat exchanger, an ERC (ejector refrigeration cycle), and a PEM (proton exchange membrane) electrolyzer, is conducted. The proposed multigeneration set-up produces refrigeration output, electricity output, heating output, and hydrogen, simultaneously. An exhaustive analytical evaluation of the introduced system is presented and findings are testified by accessible data. The findings showed that the introduced set-up yields heating load, refrigeration load, net electricity, and H_2 rate of 277 kW, 84.42 kW, 184.2 kW, and 1.433 kg/h, correspondingly.Under this circumstance, the overall energetic efficiency of the integrated system was calculated around 79.5

keywords: *Multi-generation system, Solid oxide fuel cell, Thermodynamic modeling, Parametric study.*

http://dx.doi.org/10.22109/jemt.2019.154919.1137

NOMENCLATURE

Symbols

Aa area of active surface (m^2)

AB After-burner

AC Air compressor

ERC Ejector refrigeration cycle

F Faraday constant (C/mol)

FC Fuel compressor

G Gibbs free energy (kJ)

GT Gas turbine

H specific enthalpy ($kJ.kg^{-1}$)

$HRHE$ Heat recovery heat exchanger

HX Heat exchanger

I Current (A)

j/i Current density (A/m^2)

K_p Waste gas shift reaction of equilibrium constant

LHV Lower heating value (kJ/mol)

$\dot{m}$ mass flow rate ($kg.s^{-1}$)

MGS Multigeneration system

$\dot{n}$ molar rate ($kmol.s^{-1}$)

N_{Cell} Number of fuel cells

P pressure (MPa)

PEM Proton exchange membrane

$\dot{Q}$ heat transfer rate (kW)

R_{uni} Universal gas constant ($J/mol\,K$)

S specific entropy ($kJ.kg^{-1}.K^{-1}$)

$SOFC$ Solid oxide fuel cell

T temperature (K)

U Velocity (m/s)

U_F Fuel utilization factor

V voltage (V)

$\dot{W}$ power (kW)

Subscripts and superscripts

a Anode

AC Air compressor

act activation

c cathode

$conc$ concentration

CON condenser

Dif diffuser

EJ ejector

$Elec$ electrical

EVA evaporator

EV expansion valve

exi exit

FC Fuel compressor

GT Gas turbine

i component of i

in inlet

int interconnect

is isentropic

INV DC to AC inverter

Mix mixer

Noz nozzle

net net value

ohm ohmic

out outlet

pf primary flow

PUM pump

s constant entropy

sf secondary flow

OFC Solid oxide fuel cel

th thermal

$total$ total value

$1, 2, ...$ cycle locations

0 dead state

Greek Symbols

η efficiency (

M Ejector mass entrainment ratio

Λ Membrane surface water (Q^{-1})

$\sum$ local ionic conductivity of PEM ($s.m^{-1}$)

1. INTRODUCTION

Global warming, as the most important facet of climate change through the world, pertains to the increment in the mean temperature of the oceans and atmosphere and their related effects. Currently, the climate change and its effects vary from area to area; however, the predicted impacts reveal a rising in sea levels, an increasing in global temperature, expansion of deserts, changing of precipitation, extreme weather events, etc. Global warming (GW) is supported by numerous scholars as a direct influence of greenhouse gas (GHG) emissions that faced with an upsurge trend over the recent centuries. Over the recent decades, human explorations have aggrandized the amount of GHG emissions in the ambient, where among all of them the following causes have played a significant role:

- power plants that burns fossil fuel and emits CO_2,
- transportation sections that burns gasoline and emits carbon dioxide,
- use of chemical fertilizers on croplands and
- deforesting areas like tropical forests for wood extraction.

Integrated multigeneration systems (MGSs) are energy systems which use waste heat from electrical set-ups to extracts other useful form of products, such as cooling, freshwater, heating, hydrogen, and so on. The overall thermal efficiency of a MGS is typically higher than its single-generation system. Actually, MGSs are a modified version of co- or trigeneration systems which claim great benefits [1–3].Recently, scholars have extended the MGSs for residential, industrial and commercial applications, often proposing renewable energies to decrease GHG emissions. In general, MGSs provide the following benefits [4, 5]:

- higher thermal efficiency by reducing thermal losses and wastes through the power plant,
- low operating cost,
- low GHG emissions,
- shorter transmission lines,
- fewer distribution components,
- easy exploitation of resources,
- multiple extraction capability and
- less grid failure with high reliability.

These above-mentioned profits have inspired scholars to use MGSs in place of the conventional power plants such as organic Rankine cycle (ORC) [6], cooling systems such as ejector refrigeration cycle (ERC) [7], or hydrogen production [8]. A MGS

is traditionally associated with the fossil fuels burning, but recent studies have captured different renewable energy sources, such as solar energy, geothermal heat source [9–11], solar ponds, waste thermal energy, and more interestingly, solid oxide fuel cell (SOFC) [12, 13]. With this consideration, the energetic efficiency of MGSs could be reached up to 80Among different types of fuel cells, SOFC is the most appealing one due to the following advantages [4, 21]:

- high temperature operation condition,
- great capability to bear impurities,
- providing the necessary water for the reforming reaction by a high pressure of the anode exhaust gases,
- supplying heat via convection and radiation to the endothermic reactions
- either CO and H2 can be utilized as fuel,
- no need for electrode corrosion and electrolyte loss maintenance,
- low cost for internal reforming of natural gas, and
- releasing negligible pollution.

In recent years, SOFC is used to driven various MGSs for multiple production purposes for power plants, residential applications, and other locations where different forms of output energy are required. The locations and requirements of a multigeneration system are major factors in design of its apt SOFC. In the open literature, various examinations in connection to SOFC-based multigeneration systems have been presented. On account for the technological developments and environmental concerns in the last decades, the necessity for producing multiple outputs from SOFC seems to be crucial. With this regard, Hosseini et al. [22] integrated a SOFC-GT, a SP (single-pressure)-HRSG, and a multi-effect desalination (MED) unit to produce heating, electricity, cooling, and freshwater. They designed the proposed integrated system from thermodynamic viewpoint and investigated the impacts of several central parameters on the system's efficiency. They reported performance enhancement of around 25Based upon the scrutinized literature in the above paragraphs, there are few studies investigating the feasibility of various multigeneration systems driven by SOFC as a renewable heat source. For this purpose, a new MGS driven by SOFC is proposed, developed, and analyzed from thermodynamic viewpoint for multi-productions of heating, cooling, electricity, and H_2. Later, a complete parametric examination of the devised set-up is presented. The preeminent aims of the current report can be explicitly expressed as below:

- To introduce an innovative multigeneration system ran with a SOFC cycle for multi-productions of heating, cooling, electricity, and H_2.
- To evaluate the reckoned set-up from thermodynamic viewpoint.
- To accomplish an exhaustive parametric assessment of several preeminent factors of the set-up.

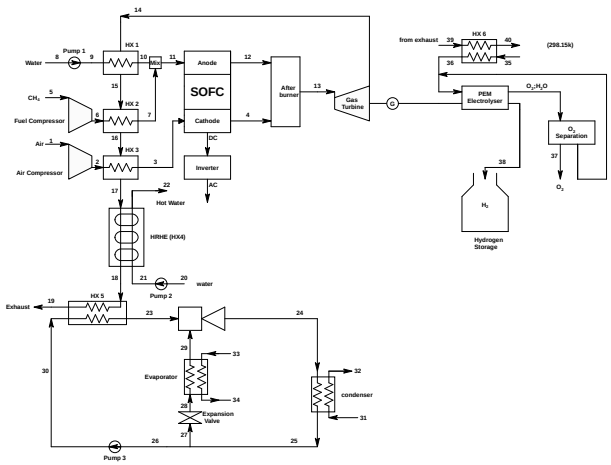

Fig. 1. Sketch of the reckoned innovative SOFC-driven multigeneration system.

2. SET-UP DESCRIPTION AND ASSUMPTIONS

Fig. 1 portrays an illustrative diagram of the introduced MGS driven by a SOFC module for power, cooling, heating, and H_2 generations. The unraveled set-up is derived from an ERC, a hybrid SOFC/GT set-up, a heat recovery heat exchanger (HRHE), and a PEM electrolyzer system. The working description of each sub-system is described in its corresponding sub-section.

A. Hybrid SOFC/GT system description

Based upon Fig. 1, the SOFC/GT system encompasses two sections as a SOFC (solid oxide fuel cell) module and a GT (gas turbine) unit. The SOFC module compromises from three heat exchangers (HXs), an AC (air compressor), a pump, an inverter, a FC (fuel compressor), an SOFC stack, and an AB (after burner). In the SOFC module, the fuel and air are pressurized via the FC and AC to the SOFC pressure, respectively and then preheated in the related heat exchangers by the exhaust of the GT. At the same time, the water is fed to the pump and then is preheated by the heat exchanger 1 to produce the preheated steam using the exhaust of the GT. Then, the fuel and steam are merged with each other to provide a mixture which drives the reforming process. The preheated air and mixture of steam and fuel enters to the cathode and anode parts of stack, respectively. Considering some reaction related to the electrochemical process, an inverter is used to convert the DC flow into AC one. After the electrochemical process, the unreacted fuel of the anode and the surplus air of the cathode combust utterly in the AB and rejects the combustion gases that are expanded trough the GT to provide electricity. Sequentially, the rejected gases from the GT are backed to the HXs to preheat H2O, fuel, and air, correspondingly.

B. HRHE description

The hot flue gases from the hybrid SOFC/GT set-up then are fed to the HRHE to produce heating capacity for heating users. The combination of GT-HRHE is proven to be a good candidate for CHP (combined heating and power) purposes by many scholars [4]. A large capacity GT requires large scale HRHE in order to ensure the ability to produce required heating capacity.

C. ERC description

The exhaust gases of the HRHE are then fed into the ERC as a thermal heat for cooling production purpose. After receiving the required heating from the exhaust gas, the ERC initiates its operation. The high saturated vapor from heat exchanger 5 outlet enters the ejector and draws the low-pressure flow into the ejector. The fluids are merged at mixing chamber and then are condensed into liquid phase. The flow is subdivided into two sections. One expanded first isenthalpically and then makes an entry to the evaporator which cools the water for cooling users. The remains are pumped back to the heat exchanger 5.

D. PEM electrolyzer description

Sketch of the PEM electrolyzer is also illustrated in Fig. 1. The necessary heat and electricity to drive the PEM electrolyzer are furnished by waste water heat and gas turbine, respectively. Specific amount of heat is used by the heat exchanger 6 (HX6) to heat the entry H_2O. Using the output electricity of the GT, H_2 exits the cathodes part while emitting dissipative thermal heat to the ambient and is chilled to the reference temperature (state 38) thereafter. The extracted O_2 is cooled down to the reference temperature (state 37). The remains are flowed to the water provision stream for the upcoming cyclic operation, accumulating hydrogen in a cylinder for disparate applications.

3. SYSTEM MODELING

A. SOFC mathematical modeling

In order to make thermodynamic evaluation of the SOFC more simple, a couple of presumptions are considered as below [25]:

- The SOFC system reaches the steady state and thermodynamic equilibrium conditions.
- The potential and kinetic energies are constant throughout the hybrid SOFC/GT analysis.
- Air molar composition is assumed 79
- The anode and cathode pressures of the SOFC are constant and equal.
- The fuel and air temperatures at the inlet of the SOFC stack are assumed equal with constant values.
- The exit flow temperature of the fuel and air in the SOFC stack is assumed equal with temperature of the SOFC.
- No heat transfer due to radiation occurs between the solid structure and gas channel.
- No gas leakage exists in the SOFC module and all gases are treated with ideal assumption.
- Contact resistances are neglected.

Either external or internal reforming processes can be taken as an advantage for a NG-based SOFC system. However, since internal reforming is reported to be a better choice compared to the external reforming [25], the internal reforming is manipulated in the current study. Hence, the reaction mechanisms taking place within the cathode and anode of the SOFC can be articulated as: Reforming:

$$CH_4 + H_2O = 3H_2 + CO \quad \textbf{(1)}$$

Table 1. A-E values used in the shifting reaction

Constant	Value
A	5.47×10^{-12}
B	-5.574×10^{-8}
C	4.6374×10^{-5}
D	-3915×10^{-2}
E	13.209723

Shifting:

$$CO + H_2O = H_2 + CO_2 \quad \textbf{(2)}$$

Electrochemical:

$$\frac{1}{2}O_2 + H_2 = H_2O \quad \textbf{(3)}$$

The shifting reaction is assumed to reach to the thermodynamic equilibrium with an equilibrium constant that may be articulated as:

$$K_p = \frac{p_{CO_2} \cdot p_{H_2}}{p_{CO} \cdot p_{H_2O}} \quad \textbf{(4)}$$

$$logK_p = AT_{SOFC}^4 + BT_{SOFC}^3 + CT_{SOFC}^2 + DT_{SOFC} + E \quad \textbf{(5)}$$

where, the values of the coefficients A-E are given in Table 1.

Presuming x, y, and z as the molar conversion rates for Eqs. (1)-(3), correspondingly, the mass balance between the inlet and exit of the SOFC may be articulated as:

$$\dot{n}_{CH_4,in} = x \quad \textbf{(6)}$$

$$\dot{n}_{H_2O,in} = 2.5x \quad \textbf{(7)}$$

$$\dot{n}_{H_2,out} = 3x + y - z \quad \textbf{(8)}$$

$$\dot{n}_{CO,out} = x - y \quad \textbf{(9)}$$

$$\dot{n}_{CO_2,out} = y \quad \textbf{(10)}$$

$$\dot{n}_{H_2O,out} = 2.5x - y + z \quad \textbf{(11)}$$

$$z = U_F\,(3x + y) \quad \textbf{(12)}$$

where, U_F is the fuel utilization factor and $\dot{n}$ stands for the molar flow rate. The cell real voltage of the SOFC may be articulated as [25]:

$$V_{SOFC} = E_r - V_{loss} \quad \textbf{(13)}$$

The electromotive force (emf), also known as the reversible cell voltage, can be obtained from the Nernst equation as follows:

$$E_r = -\frac{\Delta G^0}{n_e F} + \frac{R_{uni} T_{SOFC}}{n_e F} \ln\left(\frac{p_{H_2}\sqrt{p_{O_2}}}{p_{H_2O}}\right) \quad \textbf{(14)}$$

where, the utilized parameters are known as follows: n_e: number of the participated electrons in the electrochemical

Table 2. SOFC resistivity coefficients

i	$\delta_i(cm)$	$A_i(\Omega.cm)$	$B_i(\Omega.cm)$
Cathode	0.19	0.00814	−600
Anode	0.01	0.00298	1392
Interconnections	0.0085	0.1256	−4690
Electrolyte	0.004	0.00294	−10350

reaction, ΔG^0: the Gibbs free energy atP_0 and T_0, $R_{uni} = 8.314 J/[mol.K]$: the universal gas constant, T_SOFC: the exit temperature of the SOFC module, p: the partial pressure of different reactants, and $F = 96.458\,C/[g.mol]$: the Faraday constant. The polarization voltage loss may be articulated as:

$$V_{loss} = V_{ohm} + V_{act} + V_{conc} \tag{15}$$

where,V_{ohm}, V_{act}, V_{conc} are the ohmic polarization, activation polarization, and concentration polarization, respectively. The ohmic polarization is mostly resulted from the ionic conductivity through the electrolyte due to the interconnections. The ohmic loss of different constituents of the cell may be articulated as:

$$V_{ohm} = i\sum^{R_i} = i\sum^{\delta_i} \rho_i = i\sum^{\delta_i} A_i \exp\left(\frac{B_i}{T_{SOFC}}\right) \tag{16}$$

where, the coefficients A_i andB_i, and thickness δ_i are given in Table 2 [26].

The activation energy can be measured by the over-potential. The activation energy is supplied by both cathode and anode semi-reactions to increase speed of the overall electrochemical reaction. Thus, the activation losses can be calculated by:

$$V_{act} = V_{act,cathode} + V_{act,anode} \tag{17}$$

where,

$$V_{act,cathode} = \frac{2R_{uni}T_{SOFC}}{n_eF}\sinh^{-1}\left(\frac{i}{2i_{0,cathode}}\right) \tag{18}$$

$$V_{act,anode} = \frac{2R_{uni}T_{SOFC}}{n_eF}\sinh^{-1}\left(\frac{i}{2i_{0,anode}}\right) \tag{19}$$

where, i is the current density. The cathodic and anodic activation overvoltages can be related to the cathode and anode exchange current density by the well-known Butler-Volmer equation as follows:

$$i = i_{0,anode}\left\{\begin{array}{c} exp\left(\alpha\frac{n_eFV_{act,anode}}{R_{uni}T_{SOFC}}\right) \\ -exp\left(-(1-\alpha)\frac{n_eFV_{act,anode}}{R_{uni}T_{SOFC}}\right)\end{array}\right\} \tag{20}$$

$$i = i_{0,cathode}\left\{\begin{array}{c} exp\left(\alpha\frac{n_eFV_{act,cathode}}{R_{uni}T_{SOFC}}\right) \\ -exp\left(-(1-\alpha)\frac{n_eFV_{act,cathode}}{R_{uni}T_{SOFC}}\right)\end{array}\right\} \tag{21}$$

where, $\alpha = 0.5$ is the charge transfer coefficient. Considering transport phenomena happening in the SOFC, the concentration polarization can be taken into account. This polarization can be neglected for low current density and in general is negligible against the other polarization. Heat convection is normally negligible in concentration and only diffusion is considered in simulation. Hence, for a SOFC module with high operating temperature, the concentration polarization is small since diffusion is dominant one. In this simulation, the concentration losses are calculated by:

$$V_{conc} = V_{conc,cathode} + V_{conc,anode} \tag{22}$$

where,

$$V_{conc,cathode} = -\frac{R_{uni}T_{SOFC}}{2n_eF}\ln\left(1 - \frac{i}{2i_{conc,cathode}}\right) \tag{23}$$

$$V_{conc,anode} = -\frac{R_{uni}T_{SOFC}}{n_eF}\left\{\begin{array}{c} \ln\left(1 + \frac{p_{H_2}.\,i}{p_{H_2O}.\,i_{conc,anode}}\right) \\ -\ln\left(1 - \frac{i}{i_{conc,anode}}\right)\end{array}\right\} \tag{24}$$

$$i_{conc,cathode} = \frac{2n_e.\,F.\,p_{O_2}.\,D_{cathode,eff}}{\left(\frac{p_4 - p_{O_2,A}}{p_4}\right)R_{uni}.\,T_{SOFC}.\,L_{cathode}} \tag{25}$$

$$i_{conc,anode} = \frac{n_e.\,F.\,p_{H_2}.\,D_{anode,eff}}{R_{uni}.\,T_{SOFC}.\,L_{anode}} \tag{26}$$

where, D_{eff} is known as the effective gaseous diffusivity. The current density and current are articulated correspondingly in terms of the active surface (A_a) as below:

$$i = zn_eF/A_a \tag{27}$$

$$I_{SOFC} = i.\,A_a = zn_eF \tag{28}$$

The electrical power and inverted output power of the SOFC module may be articulated correspondingly as:

$$\dot{W}_{SOFC} = I_{SOFC}.\;V_{SOFC} \tag{29}$$

$$\dot{W}_{SOFC,Inv} = \eta_{Inv}.\,N_{cell}.\;\dot{W}_{SOFC} \tag{30}$$

where, N_{cell} is the cells number and η_{Inv} is the DC-AC inverter efficiency.

B. Ejector mathematical modeling

In the current ejector modeling, three compartments of mixer, nozzle, and diffuser are selected to accurately model ejector with corresponding efficiencies of 90

The detail mathematical formulae of the ejector are presented in Table 3 which are used from the previous published literature [29,31–33].

C. PEM electrolyzer mathematical modeling

Electrochemical modeling is employed to evaluate the PEM electrolyzer thermodynamically. The relations and presumed conditions for modeling of this component of the designed system is taken from our previous studies [11,34]. The general required energy equation in terms of the required thermal energy ($T\Delta S$) and Gibbs free energy (ΔG) is expressed as:

$$\Delta H = \Delta G + T\Delta S \tag{31}$$

More detail of thermodynamic relations for evaluation of the PEM box is presented in Table 4.

Table 3. Employed formulae for ejector modelling in the current study [29,31–33]

Name of the left-hand parameter	Formulate	Eq. number
Ejector mass entrainment ratio	$\mu = \frac{\dot{m}_{sf}}{\dot{m}_{pf}}$	(31)
Nozzle efficiency	$\eta_{Noz,is} = \frac{h_{pf,in} - h_{pf,exi}}{h_{pf,in} - h_{pf,is}}$	(32)
Primary flow exit velocity	$V_{pf,exi} = \sqrt{2\eta_{Noz}\left(h_{pf,in} - h_{pf,is}\right)}$	(33)
Momentum equation applied to the mixing chamber	$\dot{m}_{pf}V_{pf,exi} + \dot{m}_{sf}V_{sf,exi} = \left(\dot{m}_{sf} + \dot{m}_{pf}\right)V_{mf,is}$	(34)
Secondary flow exit velocity	$V_{sf,exi} = \sqrt{2 \times \left(h_{sf,in} - h_{sf,exi}\right)}$	(35)
Mixed flow velocity under isentropic condition	$V_{mf,is} = \frac{V_{pf,exi}}{1+\mu}$	(36)
Mixing chamber efficiency	$\eta_{Mix} = \frac{V_{mf}^2}{V_{mf,is}^2}$	(37)
Real velocity of the mixed flow	$V_{mf} = \frac{V_{pf,exi}\sqrt{\eta_{Mix}}}{1+\mu}$	(38)
Energy equation applied to the mixing chamber	$\dot{m}_{pf}\left(h_{pf,exi} + \frac{V_{pf,exi}^2}{2}\right) + \dot{m}_{sf}\left(h_{sf,exi} + \frac{V_{sf,exi}^2}{2}\right) = \left(\dot{m}_{sf} + \dot{m}_{pf}\right)\left(h_{mf} + \frac{V_{mf}^2}{2}\right)$	(39)
Mixed flow enthalpy	$h_{mf} = \frac{h_{pf,in} + \mu h_{sf,exi}}{1+\mu} - \frac{V_{mf}^2}{2}$	(40)
Real enthalpy of the mixed flow at exit	$h_{mf,exit} = h_{mf} + \frac{h_{mf,exi,is} - h_{mf}}{\eta_{Dif}}$	(41)
Ejector mass entrainment ratio in terms of efficiency of three different compartments	$\mu = \sqrt{\eta_{Noz}\eta_{Mix}\eta_{Dif}\left(h_{pf,in} - h_{pf,is}\right)\left(h_{mf,exi,is} - h_{mf}\right)} - 1$	(42)

D. Thermodynamic evaluation

A couple of presumptions are drawn through the energy evaluation of the introduced SOFC-driven MGS which are given as follows [36,37]:

- Steady state (SS) based equations are used.
- Refrigerant exits the evaporator and condenser at saturated vapor and liquid phases, correspondingly.
- Isenthalpic condition is governed through the expansion valves.
- Constant-based isentropic efficiencies are presumed for the compressors, pumps, and turbine.

The general-based shape of the SS-governing equations for thermodynamic evaluation of control volume may be articulated as below:

$$\sum \dot{m}_{in} - \sum \dot{m}_{out} = 0 \quad \textbf{(32)}$$

$$\sum (\dot{m}h)_{in} - \sum (\dot{m}h)_{out} + \sum \dot{Q}_{in} - \sum \dot{Q}_{out} + \dot{W} = 0 \quad \textbf{(33)}$$

The input energy rate used to drive the hybrid SOFC/GT system is declared as:

$$\dot{Q}_{in} = \dot{m}_{CH_4}.\, LHV_{CH_4} \quad \textbf{(34)}$$

where, LHV_{CH_4} stands for the lower heating value of CH_4. The isentropic efficiencies of the AC, FC, pump 1, and GT can be expressed respectively as:

$$\eta_{is,AC} = (h_{2s} - h_1) \,/\, (h_2 - h_1) \quad \textbf{(35)}$$

$$\eta_{is,FC} = (h_{6s} - h_5) \,/\, (h_6 - h_5) \quad \textbf{(36)}$$

$$\eta_{is,PUMP1} = (h_{9s} - h_8) \,/\, (h_9 - h_8) \quad \textbf{(37)}$$

$$\eta_{is,GT} = (h_{13} - h_{14}) \,/\, (h_{13} - h_{14s}) \quad \textbf{(38)}$$

Considering and applying the above mentioned isentropic efficiencies, the power of the AC, FC, pump 1, and GT can be expressed respectively as:

$$\dot{W}_{AC} = \dot{m}_1 (h_2 - h_1) \quad \textbf{(39)}$$

Table 4. Employed formulae for PEM modelling in the current study [11,34,35]

Name of the left-hand parameter	Formulae	Eq. number
H2 and H2O molar rates	$\dot{N}_{H_2,\,out} = \dot{N}_{H_2O,\,out} = \frac{J}{2F}$	(44)
PEM stack energy	$\dot{E}_{Elec} = JV$	(45)
Electric potential	$V = V_0 + V_{ohm} + V_{act,a} + V_{act,c}$	(46)
Reversible potential	$V_0 = 1.229 - 8.5 \times 10^{-4}\,(T_{PEM} - 298)$	(47)
Local ionic conductivity	$\sigma_{PEM}\,[\lambda\,(x)] = \; [0.5139\lambda\,(x) - 0.326]\,exp\left[1268\left(\frac{1}{303} - \frac{1}{T_{PEM}}\right)\right]$	(48)
Membrane surface	$\lambda\,(x) = \frac{\lambda_{\,a} - \lambda_{\,c}}{D}x + \lambda_{\,c}$	(49)
Overall resistance of PEM	$R_{\mathrm{PEM}} = \int_0^D \frac{dx}{\sigma_{\mathrm{PEM}}\,[\lambda(x)]}$	(50)
Ohmic overpotential	$V_{ohm} = JR_{PEM}$	(51)
Activation overpotential	$V_{\mathrm{act,\,i}} = \frac{RT}{F}\sinh^{-1}\left(\frac{J}{J_{0,\,i}}\right),\; i = a,\; c$	(52)
Exchange current density	$J_{0,\,i} = J_i^{ref}\,\exp\left(-\frac{E_{act,\,i}}{RT}\right),\; i = a,\; c$	(53)
Provided thermal heating	$\dot{Q}_{H_2O} = \dot{m}_{H_2O}\left(h_{out,HX6} - h_{in,HX6}\right) = \dot{m}_{H_2O}\dot{q}_{Q,PEM}$	(54)
PEM efficiency	$\eta_{th,PEM} = \frac{LHV_{H_2}\dot{N}_{H_2}}{\dot{Q}_{Q,PEM} + \dot{E}_{Elec}}$	(55)

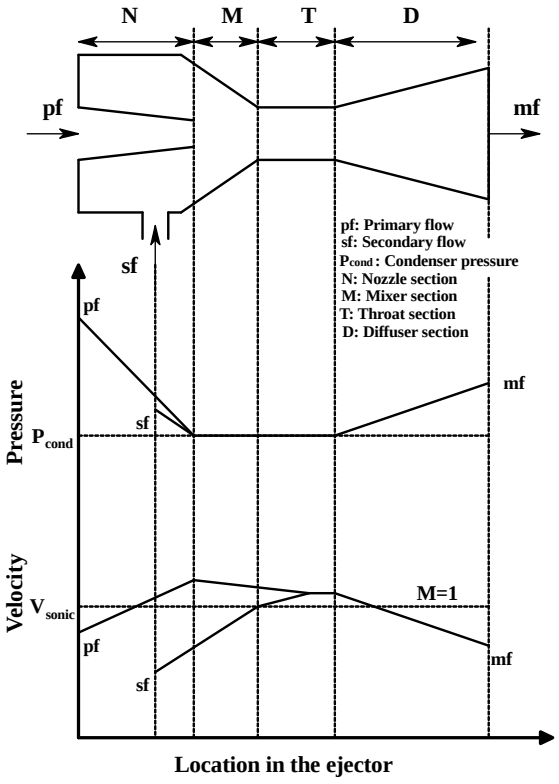

Fig. 2. Sketch of an ejector with its velocity and pressure profiles.

$$\dot{W}_{FC} = \dot{m}_5\,(h_6 - h_5) \quad \textbf{(40)}$$

$$\dot{W}_{PUMP1} = \dot{m}_9\,(h_9 - h_8) \quad \textbf{(41)}$$

$$\dot{W}_{GT} = \dot{m}_{13}\,(h_{13} - h_{14}) \quad \textbf{(42)}$$

In the recovery heat exchangers (i.e., HX1, HX2, and HX3), the energy-based balance equations are declared respectively as:
HX1:

$$\dot{Q}_{HX1} = \dot{m}_{10}\,(h_{10} - h_9) \quad \textbf{(43)}$$

$$\dot{Q}'_{HX1} = \dot{m}_{14}\,(h_{14} - h_{15}) \quad \textbf{(44)}$$

$$\eta_{HX1} = \dot{Q}_{HX1}/\dot{Q}'_{HX1} \quad \textbf{(45)}$$

HX2:

$$\dot{Q}_{HX2} = \dot{m}_7\,(h_7 - h_6) \quad \textbf{(46)}$$

$$\dot{Q}'_{HX2} = \dot{m}_{15}\,(h_{15} - h_{16}) \quad \textbf{(47)}$$

$$\eta_{HX2} = \dot{Q}_{HX2}/\dot{Q}'_{HX2} \quad \textbf{(48)}$$

HX3:

$$\dot{Q}_{HX3} = \dot{m}_3\,(h_3 - h_2) \quad \textbf{(49)}$$

$$\dot{Q}'_{HX3} = \dot{m}_{16}\,(h_{16} - h_{17}) \quad \textbf{(50)}$$

$$\eta_{HX3} = \dot{Q}_{HX3}/\dot{Q}'_{HX3} \quad \textbf{(51)}$$

Considering the heat recovery heat exchanger as a control volume, its energy-based equation is derived as:

$$\dot{Q}_{HX4} = \dot{m}_{17}\,(h_{17} - h_{18}) = \dot{m}_{22}\,(h_{22} - h_{21}) \quad \textbf{(52)}$$

Also, for pump 2 we have:

$$\eta_{is,PUMP2} = (h_{21s} - h_{20}) / (h_{21} - h_{20}) \quad (53)$$

$$\dot{W}_{PUMP2} = \dot{m}_{21} (h_{21} - h_{20}) \quad (54)$$

For HX5:

$$\dot{Q}_{HX5} = \dot{m}_{18} (h_{18} - h_{19}) = \dot{m}_{23} (h_{23} - h_{30}) \quad (55)$$

For evaporator:

$$\dot{Q}_{EVA} = \dot{m}_{29} (h_{29} - h_{28}) = \dot{m}_{33} (h_{33} - h_{34}) \quad (56)$$

For condenser

$$\dot{Q}_{COND} = \dot{m}_{25} (h_{24} - h_{25}) = \dot{m}_{32} (h_{32} - h_{31}) \quad (57)$$

For pump 3:

$$\eta_{is,PUMP3} = (h_{30s} - h_{26}) / (h_{30} - h_{26}) \quad (58)$$

$$\dot{W}_{PUMP3} = \dot{m}_{30} (h_{30} - h_{26}) \quad (59)$$

For expansion valve:

$$h_{28} = h_{27} \quad (60)$$

For HX6:

$$\dot{Q}_{HX6} = \dot{m}_{39} (h_{39} - h_{40}) = \dot{m}_{36} (h_{36} - h_{35}) \quad (61)$$

E. Overall performance criteria

For lucid comprehension from the introduced SOFC-driven MGS, the overall performance criteria established upon the first-law of thermodynamics is developed. The energetic efficiency of the introduced integrated system on account of multiple yields of cooling, heating, H_2, and power may be declared as:

$$\eta_{th} = \frac{\dot{W}_{NET} + \dot{Q}_{EVA} + \dot{Q}_{HX4} + LHV_{H_2}\dot{m}_{H_2}}{LHV_{CH_4}\dot{m}_{CH_4}} \quad (62)$$

where, $\dot{w}_{NET}$ is the net electricity and is declared as:

$$\dot{W}_{NET} = \dot{W}_{SOFC,Inv} - \dot{W}_{AC} - \dot{W}_{FC} - \dot{W}_{PUMP1} - \dot{W}_{PUMP2} - \dot{W}_{PUMP3} \quad (63)$$

4. MODEL VERIFICATION

To demonstrate accuracy of the mathematical modeling for different components of the devised set-up, it is necessary to verify our findings with those of other materials. A SS-based simulation is conducted and the findings are juxtaposed with the available numerical and experimental data. Three benchmarks are selected and derived under the same internal and external conditions. These benchmarks are ejector, PEM electrolyzer, and SOFC module, which are discussed below. In the 1st scenario, the mathematical formulae of ejector developed in the previous section is considered and juxtaposed with results of Huang et al. [38]. Table 5 draws the findings of current examination with those of Huang et al. For each case, the ejector mass entrainment ratio is fulfilled and weighed up with the 1D model and that given by Huang et al. As Table 5 signifies, the outcomes of the present modeling concur well with those of literature.

In the second benchmark, the developed analytical evaluation of PEM electrolyzer is validated with that of Ahmadi et al. [39].

Table 6. Model corroboration between current work and literature for PEM electrolyzer

Parameter	Literature	Present work	Error (%)
Net electricity (MW)	0.10196	0.101	0.5
Water pressure (bar)	1.01	1.01	0
Water temperature (K)	298	298	0
Electrolyzer exergy efficiency (%)	56.34	57.15	1.4
Exergy efficiency (%)	22.7	23.1	1.7
Energy efficiency (%)	3.6	3.75	4
H2 production rate (kg/h)	1.2	1.197	0.2

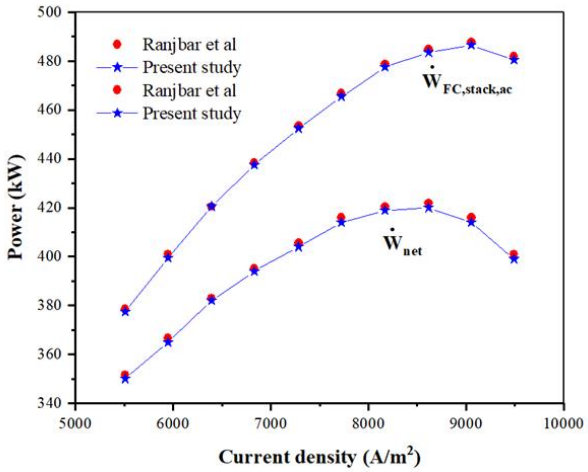

Fig. 3. Verification results between literature and present study for the hybrid SOFC/GT system.

Table 6 weighs up the findings of the current study with those of Ahmadi et al. under same conditions. For this purpose, the electrolyzing temperature is fixed at 80°C and H2 and O2 pressures are arranged at 1 atm. As Table 6 indicates, the findings of each model substantiate those of its counterpart.

Moreover, simulation of the hybrid SOFC/GT set-up is conducted as the third case study and findings are weighed up with those of Ranjbar et al. [40]. Fig. 3 illustrates alteration of SOFC and net electricity versus of the current density. For this purpose, the inlet temperature of SOFC is fixed at 1000 K and the SOFC stack temperature difference is presumed 100 K. As this figure indicates, the findings of the prevalent investigation are in good agreement with the literature.

5. RESULTS AND DISCUSSION

To numerically manipulate the simulation, it is necessary to define some main thermodynamic input parameters. Table 7 enumerated the preeminent parameters for thermodynamic evaluation of the introduced system.

Table 8 made a list of some preeminent thermodynamic

Table 5. Numerical modeling for ejector corroborated between current work and Huang et al

$P_{pf}\,(MPa)\,;T_{pf}\,()$	$P_{sf}\,(MPa)\,;T_{sf}\,()$	$T_{con}\,()$	$\mu=\dot{m}_{sf}/\dot{m}_{pf}$			Error* (%)	Error** (%)
			1-D model	Huang et al.	Present work		
0.604;95	0.04;8	42.1	0.1554	0.1859	0.1621	4.31	12.8
0.538;90	0.04;8	38.9	0.2156	0.2246	0.2201	2.08	2
0.465;84	0.04;8	35.5	0.2880	0.2880	0.2804	2.63	2.63
0.4;78	0.04;8	32.5	0.3525	0.3257	0.3334	5.41	2.36
0.604;95	0.0473;12	42.5	0.2573	0.2350	0.2402	6.64	2.21
0.538;90	0.0473;12	39.5	0.3257	0.2946	0.3023	7.18	2.91
0.465;84	0.0473;12	36	0.4147	0.3398	0.3854	7.04	13.41

Table 7. Input thermodynamic parameters for evaluation of the introduced MGS

Input parameter	Value	Input parameter	Value
Primary fluid pressure	4000	Fuel utilization factor	0.85
PPTD of HX5	30	LHV of H_2, $LHV_{H2}(kJ/kg)$	119960
Condensation temperature	300	Inverter efficiency	97
PPTD of evaporation process	3	Pressure loss of SOFC heat exchanger (%)	2
Water temperature at states 31 and 33	293	Steam/carbon ratio	2.5
Reference pressure	101.3	AB pressure loss (%)	5
Evaporation temperature	280	Average current density	5500
Reference temperature	298.1	Cell number	11000
FC isentropic efficiency	85	SOFC pressure loss (%)	2
AC pressure ratio	4	PEM Temperature	353
GT outlet pressure	113.2	O2 pressure	1.01
Pumps isentropic efficiency	85	Anode activation energy	76
GT isentropic efficiency	85	Membrane anode surface water	14
Efficiency of SOFC heat exchanger	95	Membrane thickness	10^{-4}
SOFC temperature	850	Cathode activation energy	18
AC isentropic efficiency	85	Anode pre-expotential factor	1.7×10^{5}
LHV of CH_4, $LHV_{CH4}(kJ/kg)$	50000	Membrane cathode surface water	10
LHV of CO, $LHV_{CO}(kJ/kg)$	10100	Faraday constant	96486
Combustion efficiency	99	H2 pressure	1.01
Active surface area	0.01	Cathode pre-expotential factor	4.6×10^{3}
Temperature difference between SOFC	100		

stream parameters computed from energy analysis of the introduced MGS.

Table 8. Thermodynamic stream properties for the introduced MGS

State	T (K)	P(KPa)	$h(kJ.kg^{-1})$	$s(kJ.kg^{-1}.K^{-1})$	$\dot{m}(kg.s^{-1})$
1	298.1	101.3	-0.05044	6.884	1.354
2	467	405.2	172.1	6.941	1.354
3	850	397.1	583.4	7.588	1.354
4	950	389.2	697.5	7.723	1.304
5	298.1	101.3	-4650	11.61	0.01488
6	419.6	405.2	-4355	11.72	0.01488
7	850	397.1	-2895	14.06	0.01488
8	298.1	101.3	104.6	0.3662	0.04178
9	298.1	405.2	105	0.3664	0.04178
10	850	397.1	3652	8.4	0.04178
11	850	397.1	1933	10.17	0.05666
12	950	389.2	-10380	10.76	0.1068
13	1034	369.7	61.08	8.134	1.411
14	978.6	113.2	-30.72	8.417	1.411
15	911.2	110.9	-141.3	8.338	1.411
16	901.3	108.7	-157.5	8.331	1.411
17	639.2	106.5	-573.1	7.939	1.411
18	510	104.4	-769.4	7.695	1.411
19	405	102.3	-925.1	7.452	1.411
20	293	101.3	83.3	0.294	0.8266
21	293	253.3	83.48	0.2941	0.8266
22	373	253.3	418.5	1.305	0.8266
23	480	4000	919.7	2.877	0.3388
24	385.6	369.7	758.5	2.802	0.6199
25	300	369.7	264	1.222	0.6199
26	300	369.7	264	1.222	0.3388
27	300	369.7	264	1.222	0.2812
28	280	198.5	264	1.229	0.2812
29	280	198.5	564.2	2.301	0.2812
30	302.3	4000	271.8	1.226	0.3388
31	293	101.3	83.3	0.294	6.107
32	305	101.3	133.5	0.4619	6.107
33	293	101.3	83.3	0.294	2.017
34	283	101.3	41.46	0.1487	2.017
35	298.1	101.3	104.6	0.3662	0.006707
36	353	101.3	334.3	1.073	0.006707
37	353	101.3	50.36	0.1552	0.003155
38	353	101.3	4720	55.8	0.0003981
39	369	101.3	401.6	1.26	0.0105
40	334	101.3	254.8	0.8418	0.0105

Table 9. Results of thermodynamic evaluation of the devised MGS

SOFC operating temperature,	Value
SOFC operating temperature,	950
Afterburner combustion temperature,	1034
Cell operating voltage	0.723
Power 1 consumed power,	0.014
Power 2 consumed power,	0.148
Power 3 consumed power,	2.629
AC consumed power,	233
FC consumed power,	4.389
Gas turbine output power,	129.5
SOFC electrical power,	437.5
Net output power,	184.2
Heating capacity,	277
Cooling capacity,	84.42
H2 production rate,	1.433
Overall energy efficiency,	79.57

Table 9 listed the outcomes of thermodynamic modeling for the introduced MGS under constant input parameters. Based on established data of Table 9, the net electricity, cooling load, heating load, hydrogen production rate, and energetic efficiency of the introduced MGS are obtained 184.2 kW, 84.42 kW, 277 kW, 1.433 kg/s, and 79.57

6. PARAMETRIC STUDY

Current part examines the effects of central input factors, including SOFC temperature and its current density, GT outlet pressure, compressor pressure ratio, pinch point temperature difference of HX5, ejector primary pressure, evaporation temperature, and condenser temperature on the central output operating factors including cooling load, net electricity, heating load, H2 production rate, and energetic efficiency of the set-up.

A. Effect of SOFC current density on the performance of MGS

Fig. 4 is drawn to portray change of the produced H2 rate, net electricity, cooling load, heating load, cell voltage, and energetic efficiency of the integrated set-up with various SOFC current densities. As Fig. 4(a) indicates, as SOFC current density augments, the net electricity of the set-up and extracted hydrogen rate by PEM electrolyzer are increased and decreased, respectively. Aggrandizing SOFC current density augments the flow rate of mixture through the GT, while decreasing enthalpy difference between streams. However, since the increment rate of the flue gas mass flow rate is lower than the decrement rate of enthalpy difference between the GT, thus the gas turbine output power will decline as the SOFC current density increases. Since H2 is extracted via water electrolysis through the electrolyzer and supplied power of the GT, thus the extracted hydrogen rate will drop as current density rises. Furthermore, the SOFC extracted electricity is boosted as current density augments, and hence the net electricity will augment. Fig. 4(b) illustrates variation of the produced cooling and heating capacities with various current densities of the SOFC system. Through this exhaustive investigation it is proved that the m of water through the heat exchanger 4 is increased as SOFC current density goes up, culminating in increase of the heating load. Similarly, the m of refrigerant through the evaporator of the ERC is also intensified as the SOFC current density rises, culminating in increase of the cooling load. Fig. 4(c) shows variation of the SOFC cell voltage and the system' overall energetic efficiency with various SOFC's current densities. As this figure indicates, the cell voltage is decreased as SOFC current density goes up which is predominantly because of the usual losses in the fuel cell. However, as the current density raises the system's exergetic efficiency is surged. This is potentially because of appreciable augmentation of the cooling load, heating load, and net electricity which is paramount than the decrement rate of the extracted hydrogen and increment rate of the provided fuel to the compressor.

B. Effect of SOFC inlet temperature on the performance of MGS

Fig. 5 displays change of the H2 rate, net electricity, cooling and heating loads, cell voltage, and overall exergetic efficiency with disparate SOFC inlet temperatures. Accordingly, the net electricity is maximized at $T_{in,SOFC} \approx 894.7\,K$. Thus, any design condition around this point is preferable to produce maximum electricity from the devised set-up. Meanwhile, the output electricity of the GT aggrandizes as SOFC inlet temperature increases, leading to more supply of power to the PEM, and hence extracted hydrogen rate will increase. Fig.5(b) depicts change of the heating and cooling capacities with various SOFC inlet temperatures. The heating load is declined as SOFC inlet temperature increases up to $T_{in,SOFC} \approx 828.9\,K$ and increased thereafter. Therefore, considering modeling condition around this value is not preferable from heating production viewpoint. Another paramount implication of Fig. 5(b) is alteration of the cooling capacity with disparate SOFC inlet temperatures. Based on the drawn sketch, cooling load is declined as the SOFC inlet temperature raises. This is potentially because; the secondary flow's mass flow rate through the ejector is declined as SOFC inlet temperature increases, resulting in low ejector mass entrainment ratio and cooling capacity. To show effect of the SOFC inlet temperature on its cell voltage and energetic efficiency of the set-up, Fig. **??** is plotted. As portrayed in Fig. 5(c), there is a peak point for cell voltage versus SOFC inlet temperature which is approximately at $T_{in,SOFC} \approx 907.9\,K$. Concentration and activation voltages augment as SOFC inlet temperature aggrandizes, while the ohmic voltage declines, and hence the cell voltage augments to this point and overturns thereafter. Meanwhile, the thermal efficiency decreases with $T_{in,SOFC}$ at SOFC inlet temperatures lower than $T_{in,SOFC} \approx 763.2\,K$ and increases thereafter. Therefore, a minimum thermal efficiency of 74.4

C. Effect of gas turbine outlet pressure on the devised MGS

Figure 6 is sketched to portray change of the extracted hydrogen rate, heating load, and overall energetic efficiency of the integrated system with disparate gas turbine outlet temperatures. As displayed in Fig. 6(a), the output electricity of the gas turbine decreases as gas turbine outlet pressure increases, resulting in less supply of power to the PEM and decline of extracted hydrogen rate. Decrement rate of the GT electricity is prominently because of the increment of the gas turbine outlet energy. Also, as gas turbine outlet pressure increases, the heated water's

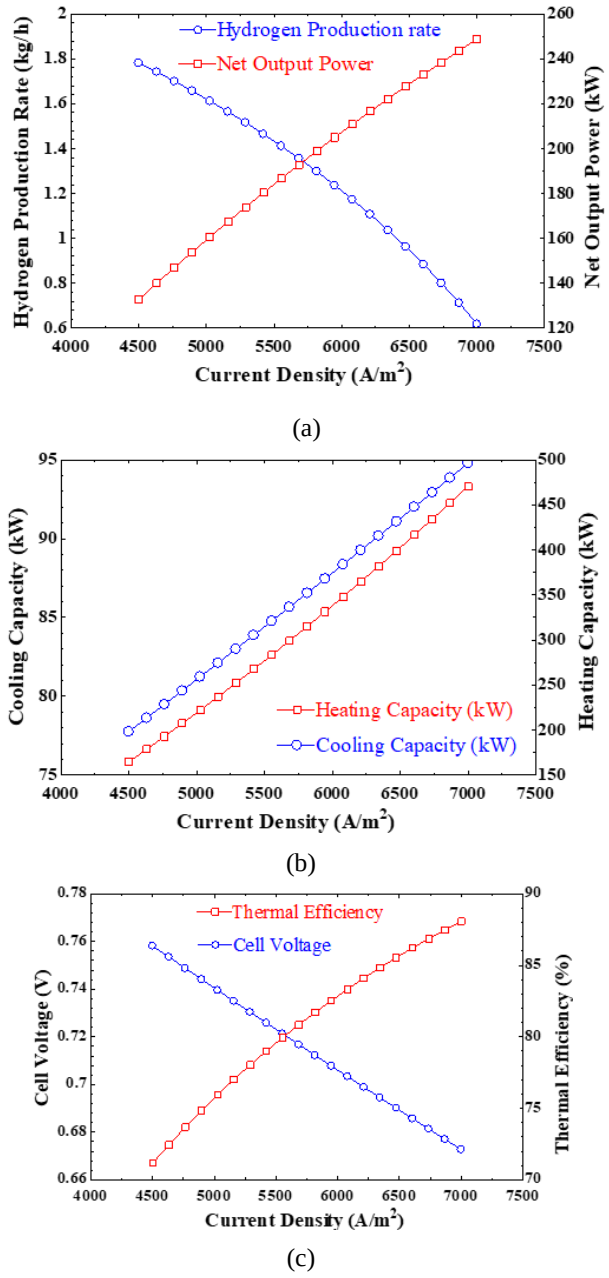

Fig. 4. Effect of SOFC current density on the: (a) H2 rate and net electricity, (b) heating capacity and cooling capacity, and (c) cell voltage and energetic efficiency.

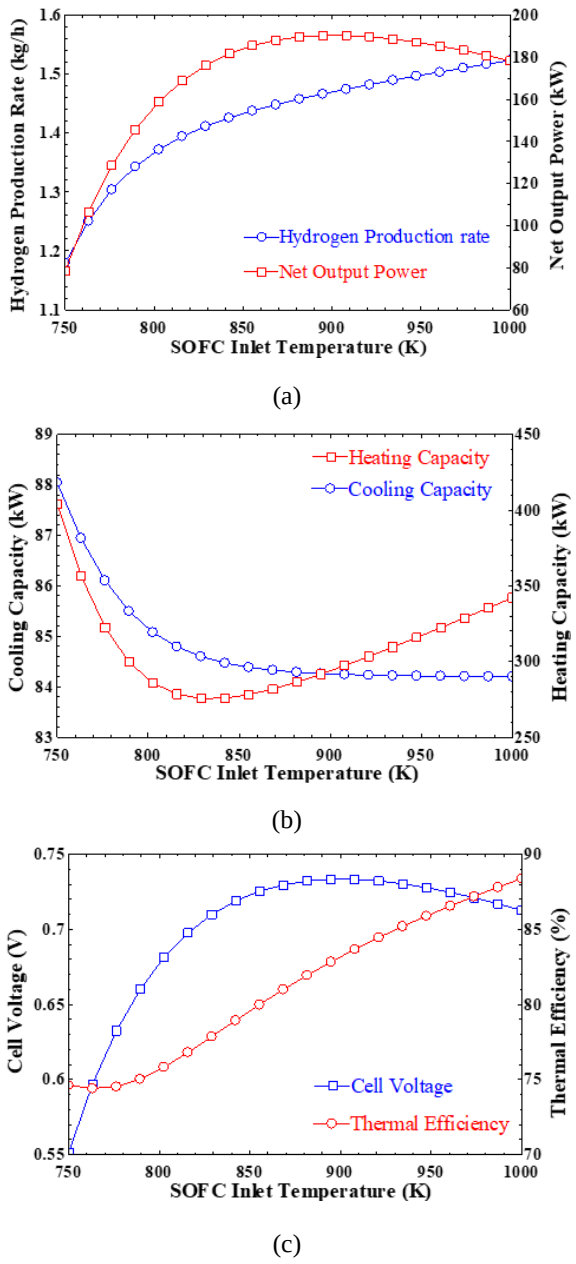

Fig. 5. Effect of $T_{in,SOFC}$ on the: (a) H2 rate and net electricity, (b) heating capacity and cooling capacity, and (c) cell voltage and energetic efficiency of the system.

flow rate through the heat exchanger 4 is augmented, and hence the heating load will be increased (Fig. 6(a)). Since decrement rate of the produced hydrogen is dominated by increasing rate of the heating load through increasing in the gas turbine outlet pressure, thus the energetic efficiency will raise during this change.

D. Effect of CPR on the devised MGS

Figure 7 portrays change of the H2 rate, net electricity, heating capacity, cell voltage, and overall energetic efficiency of the integrated set-up with disparate CPRs (compressor pressure ratios). Accordingly, the net electricity is declined as CPR increases. Meanwhile, the GT electricity increases as compressor pressure ratio increases, resulting in more electricity supply to the PEM, and hence extracted hydrogen rate will go up. Increasing the gas turbine output power is prominently because of the decrease of gas turbine outlet enthalpy which will increase the enthalpy difference across the gas turbine. Fig. 7(b) depicts alteration of the heating load and energetic efficiency with various compressor pressure ratios. As it can be perceived, the heating load is

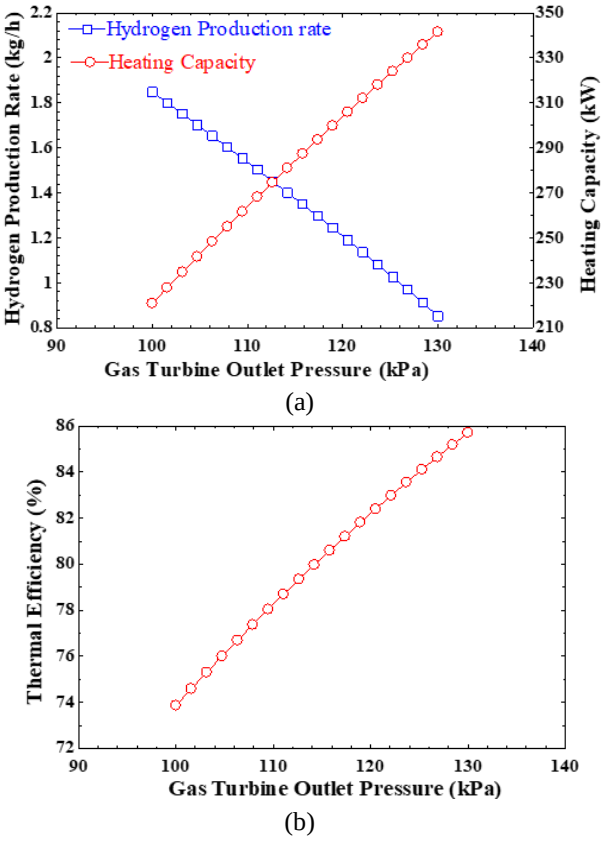

Fig. 6. Effect of GT outlet pressure on the: (a) H2 rate and heating capacity and (b) energetic efficiency of the system.

declined as CPR increases, which is prominently because of the water decrement through the heat exchanger 5. Since the heating load and net electricity decrement rates are substantially higher than the extracted H2 increment, thus the energetic efficiency will decline as CPR increases. To show effect of $T_{in,SOFC}$ on the SOFC's cell voltage, Fig. 7(c) is plotted. Accordingly, the cell voltage is increased as the compressor pressure ratio increases. This is substantially on account of the reality that the Nernst voltage considerably increased compared to other voltages (activation, ohmic and concentration voltages) as compressor pressure ratio drops, culminating in increase of the cell voltage.

E. Effect of heat exchanger 5 PPTD on the devised MGS

Figure 8 portrays the change of the cooling load, net electricity, and overall energetic efficiency with various PPTDs (pinch point temperature differences) of heat exchanger 5. Accordingly, the net electricity is subtly declined as PPTD of heat exchanger 5 increases. The trend might be explicated by the reality that as PPTD of heat exchanger 5 aggrandizes, the consumed power of pump 3 raises, therefore the net electricity will drop. Meanwhile, the cooling load is raised up as PPTD of heat exchanger 5 increases. This trend is prominently on account of the bleak water increment through the evaporator. Since the net electricity decrement is paramount than the cooling load increasing rate, therefore the energetic efficiency will surge as PPTD of heat exchanger 5 increases (Fig. 8(a)).

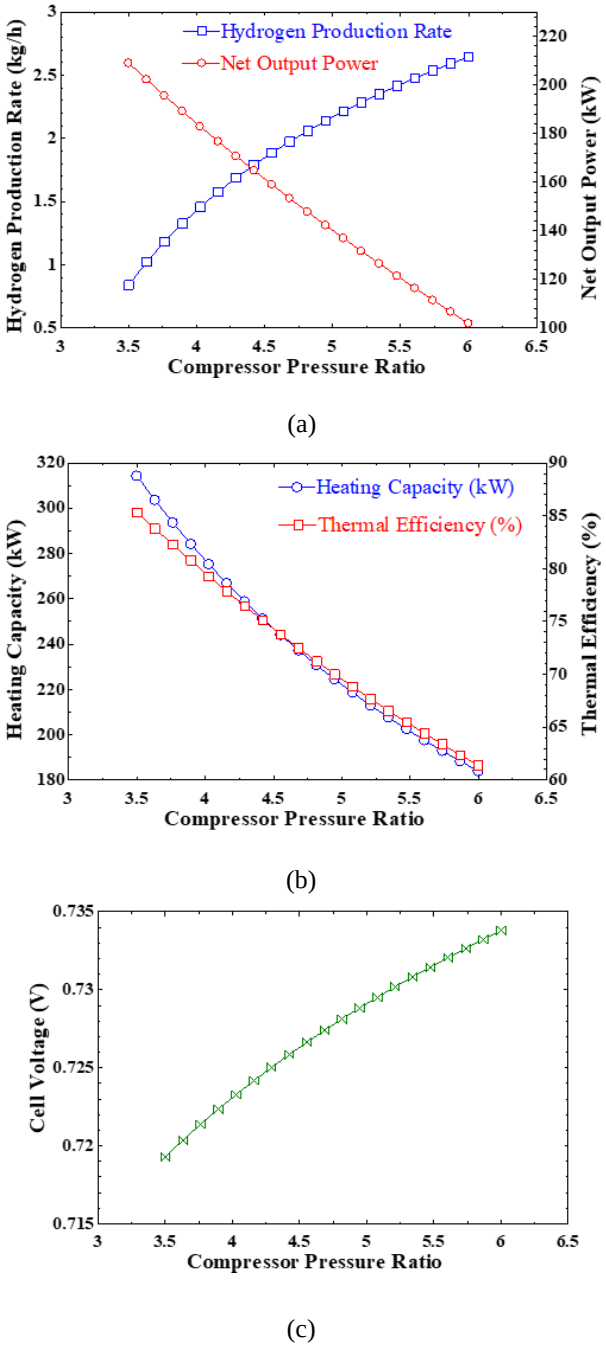

Fig. 7. Impact of CPR on the: (a) H2 rate and net electricity, (b) heating capacity and energetic efficiency of the system, and (c) cell voltage.

F. Impact of ejector primary fluid pressure on the devised MGS

Figure 9 portrays change of the cooling load, net electricity, and overall energetic efficiency of the integrated system with various ejector primary fluid (EPF) pressures. Accordingly, the net electricity is subtly declined as ejector primary fluid pressure augments. The reality might be explicated by the reality that as

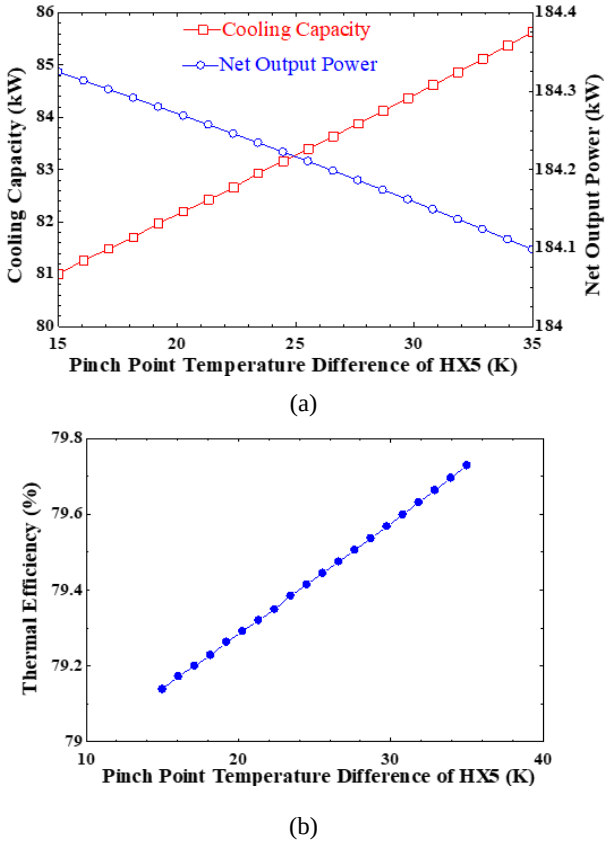

Fig. 8. Impact of PPTD of heat exchanger 5 on the: (a) net electricity and cooling load and (b) energetic efficiency of the system.

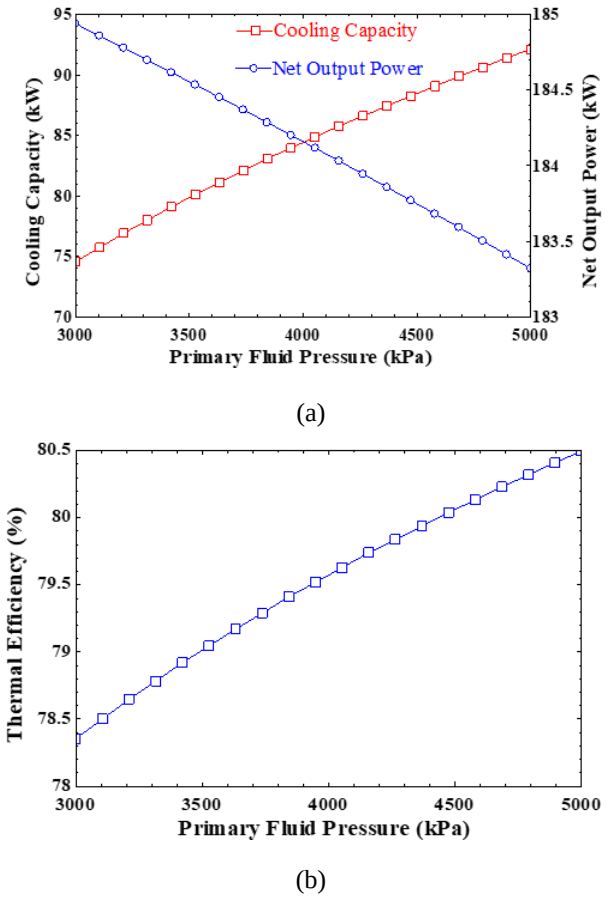

Fig. 9. Effect of ejector primary fluid pressure on the: (a) net electricity and cooling load, and (b) energetic efficiency.

ejector primary fluid pressure increases, the consumed power of pump 3 increases, and hence the net electricity will drop. From other viewpoint, the cooling load is surged as ejector primary fluid pressure augments. This trend is prominently because of the bleak water increment through the evaporator. Since the net electricity decrement is paramount than the cooling load increment, therefore the energetic efficiency will raise as ejector primary fluid pressure goes up (Fig. 9(b)).

G. Impact of condensation temperature on the devised of MGS

Figure 10 portrays change of the cooling load and overall energetic efficiency of the introduced MGS with various condensation temperatures. Accordingly, the cooling load is declined as condensation temperature goes up. This tendency is prominently due to the reality that rising condensation temperature reduces the refrigerant's mass flow rate as well as the enthalpy difference across the evaporator. Since other produced commodities (heating, hydrogen, and net power) are remained constant through varying condenser temperature, thus the thermal efficiency alteration with condenser temperature will resemble that of the cooling capacity. Therefore, the energetic efficiency will rise as condensation temperature goes up.

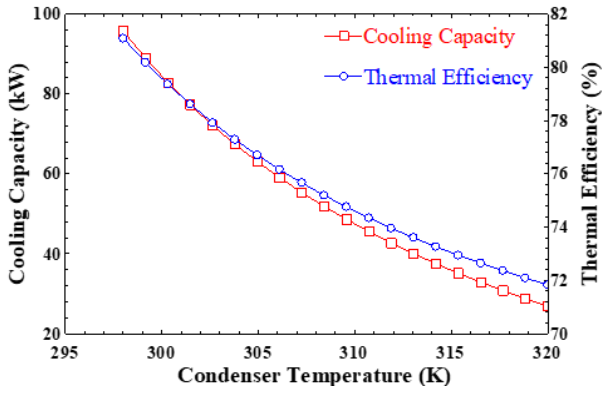

Fig. 10. Impact of condensation temperature on the energetic efficiency and cooling load.

H. Impact of evaporation temperature on the devised MGS

Figure 11 portrays change of the cooling load and overall energetic efficiency of the introduced MGS with various evaporation temperatures. Accordingly, the cooling load is gone up as evap-

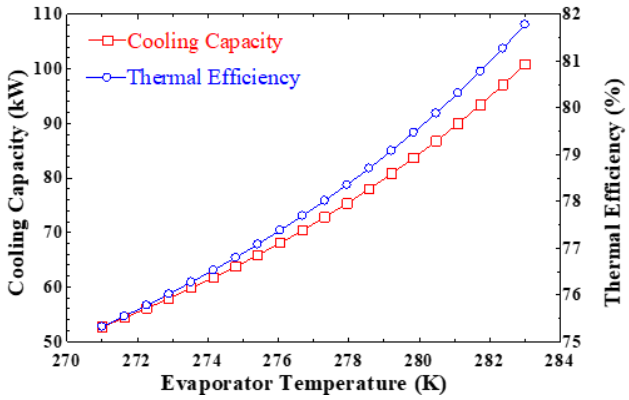

Fig. 11. Impact of evaporation temperature on the cooling load and energetic efficiency.

oration temperature rises. The preeminent reality behind this tendency is that increasing evaporator temperature augments the refrigerant's flow rate and enthalpy difference across the evaporator. Since other produced commodities (heating, hydrogen, and net power) are remained constant through varying evaporator temperature, thus the energetic efficiency alteration with evaporation temperature will resemble that of the cooling capacity. Therefore, the energetic efficiency will go up as evaporation temperature rises.

7. CONCLUSION

A thoroughgoing modeling of a new integrated set-up for multi-extraction of heating, cooling, electricity, and hydrogen is recommended in this paper. The introduced multigeneration set-up encompassed from a hybrid SOFC/GT, a heat recovery heat exchanger, a PEM stack, and an ejector refrigeration cycle. The reckoned evaluation of the recommended system is verified by available experimental and theoretical data. Synopsis of the concluding points is summarized below:

- Proposed multigeneration system produced heating load, cooling load, net electricity, and extracted hydrogen rate of 277 kW, 84.42 kW, 184.2 kW, and 1.433 kg/h, correspondingly, whilst the overall energetic efficiency of the integrated system computed 79.57
- It was discovered that a higher energetic efficiency can be fulfilled at high SOFC current densities, SOFC inlet temperatures, gas turbine outlet pressures, pinch point temperature differences of heat exchanger 5, ejector primary fluid pressures, and evaporating temperatures or low compressor pressure ratios and condensing temperatures.
- It was discovered that higher electricity can be produced at high SOFC current densities, or low compressor pressure ratios and pinch point temperature differences of heat exchanger 5, and ejector primary fluid pressures.
- It was concluded that higher hydrogen can be produced at high SOFC inlet temperatures and compressor pressure ratios or low gas turbine outlet pressures and SOFC current densities.
- It was concluded that paramount amount of cooling load can be produced at high SOFC current densities, pinch point temperature differences of heat exchanger 5, ejector primary fluid pressures, and evaporating temperatures or low SOFC inlet temperatures and condensing temperatures.
- It was concluded that paramount amount of heating load can be produced at high SOFC current densities and gas turbine outlet pressures or low compressor pressure ratios.
- Performance of the introduced system can reach to a pinnacle versus of the SOFC inlet temperature.

REFERENCES

1. H. Ghaebi, H. Rostamzadeh, and P. S. Matin, "Performance evaluation of ejector expansion combined cooling and power cycles," Heat and Mass Transfer, vol. 53, pp. 2915-2931, 2017.
2. H. Rostamzadeh, H. Ghaebi, and F. Behnam, "Energetic and exergetic analyses of modified combined power and ejector refrigeration cycles," Thermal Science and Engineering Progress, vol. 2, pp. 119-139, 2017.
3. H. Rostamzadeh, M. Ebadollahi, H. Ghaebi, M. Amidpour, and R. Kheiri, "Energy and exergy analysis of novel combined cooling and power (CCP) cycles," Applied Thermal Engineering, vol. 124, pp. 152-169, 2017.
4. P. Ahmadi, "Modeling, analysis and optimization of integrated energy systems for multigeneration purposes," 2013.
5. I. Dincer and C. Zamfirescu, "Renewableenergybased multigeneration systems," International Journal of Energy Research, vol. 36, pp. 1403-1415, 2012.
6. H. Ghaebi, H. Rostamzadeh, J. Rostamzadeh, M. Ebadolahi, and H. Abioghli, "Comparison of Different Working Fluids Operation for Basic and Modified Organic Rankine Cycles (ORCs)," Journal of Energy Management and Technology, vol. 2, pp. 25-31, 2018.
7. M. Ebadollahi, H. Rostamzadeh, H. Ghaebi, M. Amidpour, F. Rostamian, and H. Abioghli, "Energy analysis and performance Evaluation of a novel multi evaporator Ejector Refrigeration Cycle (ERC)," Journal of Energy Management and Technology, vol. 1, pp. 38-45, 2017.
8. H. R. Lari and M. R. Shahnazari, "Experimental investigation of Methane Partial Oxidation for Hydrogen Production," Journal of Energy Management and Technology, vol. 2, pp. 20-28, 2018.
9. H. Rostamzadeh, S. G. Gargari, A. S. Namin, and H. Ghaebi, "A novel multigeneration system driven by a hybrid biogas-geothermal heat source, Part I: Thermodynamic modeling," Energy Conversion and Management, vol. 177, pp. 535-562, 2018.
10. H. Rostamzadeh, S. G. Gargari, A. S. Namin, and H. Ghaebi, "A novel multigeneration system driven by a hybrid biogas-geothermal heat source, Part II: Multi-criteria optimization," Energy Conversion and Management, vol. 180, pp. 859-888, 2019.

11. M. Ebadollahi, H. Rostamzadeh, M. Z. Pedram, H. Ghaebi, and M. Amidpour, "Proposal and assessment of a new geothermal-based multigeneration system for cooling, heating, power, and hydrogen production, using LNG cold energy recovery," Renewable Energy, 2018.

12. H. Rostamzadeh, H. Ghaebi, and K. Mostoufi, "Theoretical analysis of a novel combined cooling, heating, and power (CCHP) cycle," Energy Equipment and Systems, vol. 5, pp. 241-249, 2017.

13. H. Ghaebi, T. Parikhani, and H. Rostamzadeh, "A novel trigeneration system using geothermal heat source and liquefied natural gas cold energy recovery: Energy, exergy and exergoeconomic analysis," Renewable Energy, vol. 119, pp. 513-527, 2018.

14. A. Khaliq, R. Kumar, and I. Dincer, "Performance analysis of an industrial waste heatbased trigeneration system," International Journal of Energy Research, vol. 33, pp. 737-744, 2009.

15. H. Ghaebi, A. S. Namin, and H. Rostamzadeh, "Performance assessment and optimization of a novel multi-generation system from thermodynamic and thermoeconomic viewpoints," Energy Conversion and Management, vol. 165, pp. 419-439, 2018.

16. Y. E. Yuksel, M. Ozturk, and I. Dincer, "Energetic and exergetic performance evaluations of a geothermal power plant based integrated system for hydrogen production," International Journal of Hydrogen Energy, vol. 43, pp. 78-90, 2018.

17. Y. E. Yuksel, M. Ozturk, and I. Dincer, "Energetic and exergetic performance evaluations of a geothermal power plant based integrated system for hydrogen production," International Journal of Hydrogen Energy, vol. 43, pp. 78-90, 2018.

18. R. Soltani, I. Dincer, and M. A. Rosen, "Thermodynamic analysis of a novel multigeneration energy system based on heat recovery from a biomass CHP cycle," Applied Thermal Engineering, vol. 89, pp. 90-100, 2015.

19. Y. E. Yuksel and M. Ozturk, "Energy and exergy analyses of an integrated solar and biomass-assisted multi-generation system with hydrogen production," International Journal of Exergy, vol. 20, pp. 203-235, 2016.

20. M. S. Azhar, G. Rizvi, and I. Dincer, "Integration of renewable energy based multigeneration system with desalination," Desalination, vol. 404, pp. 72-78, 2017.

21. "Essays, UK. (November 2013). Advantages And Disadvantages Of Solid Oxide Fuel Cells Engineering Essay. Retrieved from https://www.ukessays.com/essays/engineering/advantages-and-disadvantages-of-solid-oxide-fuel-cells-engineering-essay.php?vref=1

22. M. Hosseini, I. Dincer, P. Ahmadi, H. B. Avval, and M. Ziaasharhagh, "Thermodynamic modelling of an integrated solid oxide fuel cell and micro gas turbine system for desalination purposes," International Journal of Energy Research, vol. 37, pp. 426-434, 2013.

23. Y. Bicer and I. Dincer, "Energy and exergy analyses of an integrated underground coal gasification with SOFC fuel cell system for multigeneration including hydrogen production," International Journal of Hydrogen Energy, vol. 40, pp. 13323-13337, 2015.

24. O. Siddiqui and I. Dincer, "Analysis and performance assessment of a new solar-based multigeneration system integrated with ammonia fuel cell and solid oxide fuel cell-gas turbine combined cycle," Journal of Power Sources, vol. 370, pp. 138-154, 2017.

25. S. Ma, J. Wang, Z. Yan, Y. Dai, and B. Lu, "Thermodynamic analysis of a new combined cooling, heat and power system driven by solid oxide fuel cell based on ammonia–water mixture," Journal of Power Sources, vol. 196, pp. 8463-8471, 2011.

26. F. Calise, A. Palombo, and L. Vanoli, "Design and partial load exergy analysis of hybrid SOFC–GT power plant," Journal of power sources, vol. 158, pp. 225-244, 2006.

27. H. Rostamzadeh, H. Ghaebi, S. Vosoughi, and J. Jannatkhah, "Thermodynamic and thermoeconomic analysis and optimization of a novel dual-loop power/refrigeration cycle," Applied Thermal Engineering, vol. 138, pp. 1-17, 2018.

28. H. Rostamzadeh, H. Ghaebi, and T. Parikhani, "Thermodynamic and thermoeconomic analysis of a novel combined cooling and power (CCP) cycle," Applied Thermal Engineering, 2018.

29. H. Rostamzadeh, J. Rostamzadeh, P. S. Matin, and H. Ghaebi, "Novel dual-loop bi-evaporator vapor compression refrigeration cycles for freezing and air-conditioning applications," Applied Thermal Engineering, 2018.

30. M. Ebadollahi, H. Rostamzadeh, P. S. Matin, H. Ghaebi, and M. Amidpour, "Performance Evaluation of Ejector Refrigeration Cycle (ERC) Using Multi-parallel Ejectors," 2017.

31. H. Rostamzadeh, M. Ebadollahi, H. Ghaebi, and A. Shokri, "Comparative study of two novel micro-CCHP systems based on organic Rankine cycle and Kalina cycle," Energy Conversion and Management, vol. 183, pp. 210-229, 2019.

32. H. Rostamzadeh, K. Mostoufi, M. Ebadollahi, H. Ghaebi, and M. Amidpour, "Exergoeconomic optimisation of basic and regenerative triple-evaporator combined power and refrigeration cycles," International Journal of Exergy, vol. 26, pp. 186-225, 2018.

33. H. Ghaebi, T. Parikhani, H. Rostamzadeh, and B. Farhang, "Thermodynamic and thermoeconomic analysis and optimization of a novel combined cooling and power (CCP) cycle by integrating of ejector refrigeration and Kalina cycles," Energy, vol. 139, pp. 262-276, 2017.

34. H. Ghaebi, B. Farhang, H. Rostamzadeh, and T. Parikhani, "Energy, exergy, economic and environmental (4E) analysis of using city gate station (CGS) heater waste for power and hydrogen production: A comparative study," International Journal of Hydrogen Energy, vol. 43, pp. 1855-1874, 2018.

35. M. Ni, M. K. Leung, and D. Y. Leung, "Energy and exergy analysis of hydrogen production by a proton exchange membrane (PEM) electrolyzer plant," Energy conversion and management, vol. 49, pp. 2748-2756, 2008.

36. H. Ghaebi, T. Parikhani, and H. Rostamzadeh, "Energy, exergy and thermoeconomic analysis of a novel combined cooling and power system using low-temperature heat source and LNG cold energy recovery," Energy Conversion and Management, vol. 150, pp. 678-692, 2017.

37. T. Parikhani, H. Ghaebi, and H. Rostamzadeh, "A novel geothermal combined cooling and power cycle based on the absorption power cycle: Energy, exergy and exergoeconomic analysis," Energy, vol. 153, pp. 265-277, 2018.

38. B. Huang, J. Chang, C. Wang, and V. Petrenko, "A 1-D analysis of ejector performance," International journal of refrigeration, vol. 22, pp. 354-364, 1999.

39. P. Ahmadi, I. Dincer, and M. A. Rosen, "Energy and exergy analyses of hydrogen production via solar-boosted ocean thermal energy conversion and PEM electrolysis," International Journal of Hydrogen Energy, vol. 38, pp. 1795-1805, 2013.

40. F. Ranjbar, A. Chitsaz, S. Mahmoudi, S. Khalilarya, and M. A. Rosen, "Energy and exergy assessments of a novel trigeneration system based on a solid oxide fuel cell," Energy Conversion and Management, vol. 87, pp. 318-327, 2014.